Nanoscale Advances

ROYAL SOCIETY OF CHEMISTRY

COMMUNICATION

View Article Online
View Journal | View Issue

Cite this: *Nanoscale Adv.*, 2025, **7**, 6791

Unveiling the supercapacitive behavior of electrospun Cr_2CT_x/carbon nanofiber membrane

R. Madhushree, [ab] K. R. Sunajadevi, *[ab] K. P. Chaithra, [ab] T. P. Vinod *[ab] and B. Saravanakumar [c]

Received 7th August 2025
Accepted 30th September 2025

DOI: 10.1039/d5na00753d

rsc.li/nanoscale-advances

A novel electrospinning-based strategy was employed to fabricate Cr_2CT_x/carbon nanofibers using Cr_2CT_x MXene and polyvinyl alcohol (PVA) as precursors. This approach enables the formation of porous, conductive composite MXene layers dispersed in carbon nanofibers. The resulting material exhibited notable supercapacitive performance, delivering 338.8 F g^{-1} capacitance, 67.7 Wh kg^{-1} energy, and 1998 W kg^{-1} power density.

In the quest for next-generation energy storage systems, supercapacitors (SCs) have garnered interest for their swift charge–discharge behavior, superior power density, and cycling stability.[1] Among the various materials explored, two-dimensional MXenes, represented by the formula $M_{n+1}X_nT_x$, where M represents transition metals, X can be C, N, B, or carbonitride, and T_x refers to the attached terminating groups, have recently emerged as promising candidates for electrodes. Particularly, carbide-derived MXenes such as $Ti_3C_3T_x$, Mo_2CT_x, and Cr_2CT_x demonstrate remarkable electrical conductivity ($\sim 10^4$ S cm^{-1}), thermal robustness, and tunable surface characteristics, making them excellent candidates for high-rate energy storage applications.[2–4] These attributes position carbide-based MXenes as front-runners in the development of advanced SCs capable of delivering both high performance and reliability.[5]

Several studies have explored the integration of Ti-based MXenes with carbon nanofiber (CNF) matrices and various modifiers to enhance supercapacitor performance. Levitt *et al.* designed a free-standing Ti MXene/CNF electrode through an electrospinning technique using polyacrylonitrile (PAN) as the polymer matrix, achieving a capacitance of 205 mF cm^{-2} at 50 mV s^{-1}.[6] Subsequently, Zhao *et al.* modified Ti-based MXene with rGO and poly(3,4-ethylenedioxythiophene) (PEDOT): polystyrene sulfonate (PSS) *via* hydrothermal self-assembly, followed by radical freezing and drying. The resulting hybrid electrode delivered a capacitance of 113 F g^{-1} at 0.2 A g^{-1} in an asymmetric device configuration.[7] In another approach, Ti-MXene was combined with MnO_2 and carbon nanotube (CNT) *via* wet spinning to form a flexible film, which was investigated for supercapacitance application.[8] Moreover, a Co-MOF modified MnO_2/MXene/CNF composite was developed through electrospinning followed by carbonization, demonstrating battery-type behavior with enhanced electrochemical performance.[9] Hwang *et al.* outlined the synthesis of an electrospun Ti-MXene/CNF composite that exhibited notable cyclic stability, preserving 98% of its starting capacitance through 10 000 cycles.[10] Similarly, Xue Yan *et al.* modified MXene with $FeCo_2S_4$ and embedded it into a carbon nanofiber matrix derived from PAN, utilizing polyvinylpyrrolidone (PVP) as a pore-forming sacrificial agent. The resulting composite showed promising supercapacitance performance.[11] A polyaniline (PANI)/MXene/CNF composite with an entangled nanofibrous morphology achieved a capacitance of 356 F g^{-1} in an acidic medium at 0.5 A g^{-1}.[12] Beyond energy storage, MXene/polycaprolactone (PCL) electrospun fibers have been explored for biomedical applications, demonstrating the versatility of MXene-based nanocomposites.[13] To date, no studies have documented the incorporation of Cr-based MXene embedded in carbon nanofibers. In this work, we pioneer the development of electrospun Cr_2CT_x/carbon nanofibers composite, moving beyond Ti-based MXenes. A simple electrospinning technique was employed, with polyvinyl alcohol (PVA) chosen as a sustainable polymer precursor due to its cost-effectiveness, hydrophilicity, excellent catalyst dispersion, and superior biocompatibility compared to other polymers. The resulting material exhibits improved thermal stability and demonstrates excellent performance as an electrode for supercapacitor applications, which accounts for SDG 7, clean and affordable energy.

The chemicals utilized in the present study are summarized in Table S1. The two-step synthetic procedure for Cr_2CT_x/carbon

[a]*Department of Chemistry, Christ University, Bengaluru, 560029, India. E-mail: sunajadevi.kr@christuniversity.in; vinod.tp@christuniversity.in*

[b]*Centre for Renewable Energy and Environmental Sustainability, Christ University, Bengaluru, 560029, India*

[c]*Department of Physics, Dr Mahalingam College of Engineering and Technology, Pollachi, Tamil Nadu 642003, India*

nanofibers, adapted from a reported protocol,[14,15] is illustrated in Fig. S1a. In brief, Cr_2CT_x MXene was derived from the Cr_2AlC *via* chemical etching. A 0.5% w/v MXene solution was prepared by probe sonication, followed by the addition of 10% w/v PVA. The mixture was then heated and stirred at 90 °C for 4 h to achieve uniformity, resulting in a homogeneous spinning solution. The Cr_2CT_x/carbon nanofibers were fabricated *via* electrospinning under optimized conditions (25 kV, needle-to-collector distance of 18 cm, and 0.5 mL h^{-1} were maintained at 25 °C and 40% humidity), followed by carbonization at 300 °C for 1 h.[15] Table S2 outlines the characterization methods employed to confirm the formation of Cr_2CT_x/carbon nanofibers. Structural analysis through XRD (Fig. S1b) shows the distinct diffraction peaks of Cr_2CT_x (black trace), consistent with JCPDS Card no. 29-0017 and prior reports.[16–18] The XRD spectra of Cr_2CT_x/carbon nanofibers further support the incorporation of MXene layers. The asterisks (*) mark residual crystalline MXene peaks observed at 13.8° (002), 26.5° (004), 35.1° (100), 43.1° (104), 54.6° (106), and 56.8°, alongside a broad hump between 15°–30°, characteristic of amorphous carbon (carbon nanofibers). The noticeable reduction in peak intensity of the aforementioned peaks suggests reduced crystallinity and confirms the successful integration of carbon nanofibers (purple trace).

Raman spectra for both samples are shown in Fig. S1c. In Cr_2CT_x MXene (black trace), the D-band at 1348 cm^{-1} indicates carbon defects, and the G-band at 1574 cm^{-1} corresponds to graphitic carbon, with an I_D/I_G ratio of 0.85. Additionally, a peak at 2702 cm^{-1} corresponds to Cr–C/O–H stretching vibration.[19] In Cr_2CT_x/carbon nanofiber spectrum (purple trace) exhibits D- and G-bands at 1398 cm^{-1} and 1595 cm^{-1}, respectively, with a higher I_D/I_G ratio of 0.87 to the carbonization during synthesis. The slight increase in I_D/I_G ratio suggests enhanced defect density and active sites, thereby aiding improved charge storage and electrochemical efficiency in the supercapacitor. The specific surface area of Cr_2CT_x/carbon nanofiber, measured *via* BET analysis, was found to be 6.65 $m^2\ g^{-1}$ (Fig. S1d). The N_2 adsorption–desorption isotherm corresponds to Type III behaviour with an H_3 hysteresis loop. BJH data further revealed a mesoporous structure with a pore diameter of 2.43 nm and a pore volume of 0.0188 $cm^3\ g^{-1}$ (Fig. S1d: inset). Further, the morphological and elemental composition of the samples was confirmed by SEM-EDX analysis. The multi-layered structure characterization of Cr_2CT_x is clearly observed in Fig. S1e. The Cr_2CT_x/carbon nanofiber morphology, illustrated at different magnifications (3 μm, 1 μm, and 500 nm), reveals a homogeneous, continuous, and interconnected network with an average fiber diameter of 209 ± 52 nm (Fig. S1g and h). Fig. S2a and b indicates the SEM images of the cross-sectional view of Cr_2CT_x/carbon nanofiber composite, illustrating the well-dispersed MXene sheets within the CNF network. The histogram showing the fiber diameter distribution is presented in Fig. S2c. Additionally, the thermogravimetric analysis (TGA) curves of PVA and Cr_2CT_x/carbon nanofiber are compared, demonstrating enhanced thermal stability of the composite, with a residual mass of 59.1%. The pristine Cr_2CT_x MXene and composite's elemental compositions are illustrated in Fig. S3a and b, confirming the presence of carbon, oxygen, and chromium. In the Cr_2CT_x/carbon nanofiber, despite initially incorporating 0.5% of Cr_2CT_x, the EDX analysis shows a Cr content of 4.99 wt%. The increase in Cr content is attributed to the retention and enrichment of Cr during the carbonization process, as well as the contribution from Cr sputtering. The sputtering effect was carefully assessed using carbon paper, which indicated an additional contribution of approximately 2.15 wt% Cr, helping to explain the overall higher Cr content observed. This is attributed to the carbonized PVA matrix, partial encapsulation of Cr_2CT_x inside the CNFs, and the surface-sensitive nature of EDX measurements. Fig. S3c further confirms the elemental composition through EDS elemental mapping, showing a uniform distribution of carbon resulting from the carbonization process. Oxygen is present due to the use of a static air atmosphere, which helps create additional defect sites, while the relatively lower chromium signal corresponds to its low initial loading in the composite. These results verify the successful integration of Cr_2CT_x within the nanofiber matrix. Such a well-connected network structure is expected to facilitate efficient charge transport, enhancing the electrochemical performance.

The electrochemical behavior of Cr_2CT_x/carbon nanofiber was investigated using a CHI608E electrochemical testing unit. Cyclic voltammetry (CV), galvanostatic charge–discharge (GCD), and electrochemical impedance spectroscopy (EIS) measurements were conducted in a three-electrode configuration, employing 3 M KOH as the electrolyte. Comprehensive information regarding electrode preparation can be found in the SI under the section titled electrode fabrication. Fig. 1a and b presents the CV profiles of the samples recorded at a scan rate of 200–10 mV s^{-1} and 10–1 mV s^{-1}, displaying a typical pseudocapacitor-type CV profile with well-defined redox activity, where the charge storage arises not only from the double-layer capacitance but also from rapid faradaic reactions occurring at the electrode surface. The redox peaks observed at 0.45 V and 0.29 V correspond to reversible faradaic reactions involving the intercalation and deintercalation of electrolyte ions into the Cr_2CT_x/CNF composite. In addition, the CNF matrix contributes electric double-layer capacitance and may also enhance pseudocapacitive behavior through surface functional groups (–OH, =O) present on the MXene. The combination of these processes leads to the quasi-rectangular shape of the CV curves, along with clearly defined redox peaks, indicating a dominant pseudocapacitive charge storage mechanism.

As the scan rate increases from 1 mV s^{-1} to 10 mV s^{-1}, the current response increases and the redox peaks remain visible, indicating good rate capability and preserved pseudocapacitive characteristics.[20]

To elucidate the charge storage dynamics and underlying electrochemical processes, the *b*-values were calculated using eqn (S1) by plotting $\log(i_p)$ *vs.* $\log(v)$. A *b*-value of 0.622 was observed for the MXene electrode, reflecting a combination of surface and diffusion-controlled charge storage behavior. In contrast, the Cr_2CT_x/carbon nanofiber composite electrode demonstrated a slightly higher *b*-value of 0.687, the observed diffusion-limited behavior, coupled with minor capacitive

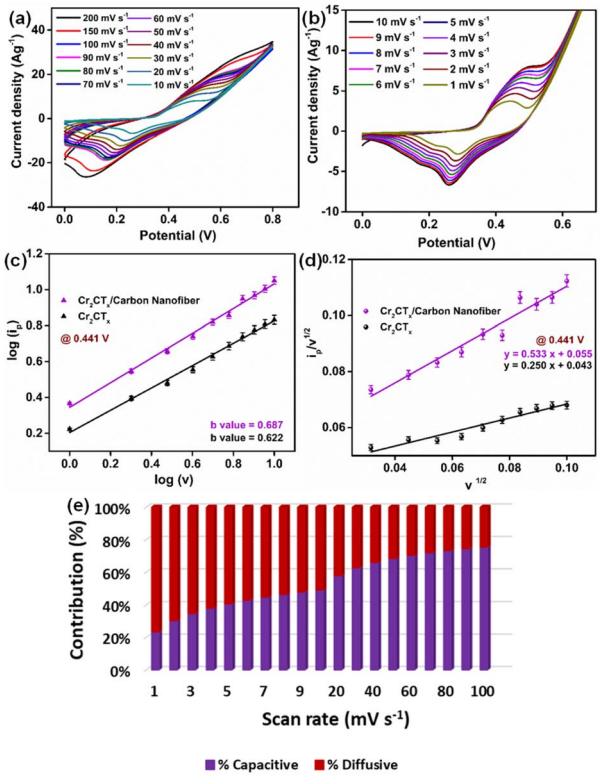

Fig. 1 CVs recorded at: (a) high scan rate range from 200 to 10 mV s^{-1}, (b) low scan rate range from 10 to 1 mV s^{-1}, (c) *b*-value plot, (d) intercept plot, and (e) surface-controlled and diffusion-limited contributions across various scan rates.

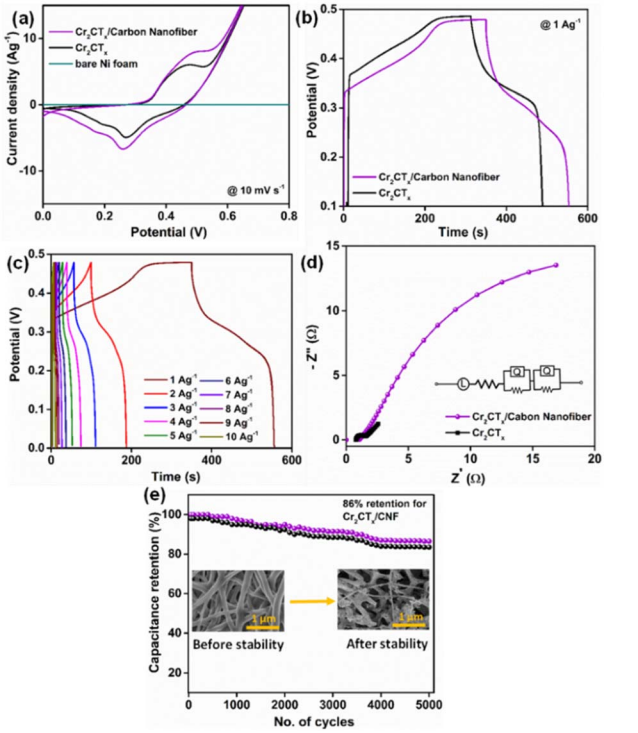

Fig. 2 (a) CV profiles of as-synthesised materials at 10 mV s^{-1}, (b) GCD comparative performance plots of Cr_2CT_x/carbon nanofiber and Cr_2CT_x at 1 A g^{-1}, (c) GCD curves recorded at different current density for Cr_2CT_x/carbon nanofiber, (d) Nyquist plot (inset: fitted Randels circuit), and (e) cycling stability (inset: morphology before and after stability), all measured using a three-electrode system.

contribution, can be attributed to the porous nanofibrous framework, which aids in efficient ion transport and enables surface-confined redox reactions (Fig. 1c). To further validate these results, using eqn (S2), capacitive (m_1v) and diffusive contributions ($m_2v^{1/2}$) were determined by plotting $\frac{i_p}{v^{1/2}}$ and $v^{1/2}$ (Fig. 1d). For Cr_2CT_x/carbon nanofiber, the slope (m_1) and *y*-intercept (m_2) were found to be 0.533 and 0.055, respectively, enabling quantification of the charge storage contributions at various scan rates (Fig. 1e).

At 1 mV s^{-1}, the composite exhibited 76.52% diffusion-controlled and 23.47% capacitive contributions, confirming a predominantly diffusion-controlled mechanism. As the scan rate increased from 1 to 100 mV s^{-1}, the diffusion contribution decreased from 76.52% to 6.19%, while the capacitive contribution rose from 23.47% to 75.41%, reflecting the limited time available for ion diffusion at higher scan rates and the dominant role of surface-controlled processes. Overall, the enhanced electrochemical performance of the Cr_2CT_x/carbon nanofiber can be primarily due to its synergistic architecture, where the interconnected porous nanofibers enhance electrolyte accessibility, ion diffusion, and surface redox activity, resulting in improved capacitive behavior and rate capability.

Further, Fig. 2a compares the CV profiles of pristine Cr_2CT_x MXene and Cr_2CT_x/carbon nanofiber at 10 mV s^{-1}, recorded in a potential window of 0 to 0.8 V. It is hypothesized that the carbon matrix provides protective shielding, allowing the electrodes to operate efficiently at higher positive potentials.[6] The composite exhibits a larger CV area, reflecting its superior charge storage capacity and enhanced electrochemical performance. The GCD profiles presented in Fig. 2b and c further highlight distinctive pseudocapacitive characteristics and charge storage capabilities. The GCD curves for Cr_2CT_x/carbon nanofiber (purple trace) and Cr_2CT_x (black trace) were recorded at a current density of 1 A g^{-1} within a potential window of 0.1–0.48 V (Fig. 2b). Both profiles exhibit the characteristic quasi-triangular shapes of pseudocapacitors, with slight deviations indicating a combined contribution from faradaic redox reactions and capacitive charge storage.

The Cr_2CT_x/carbon nanofiber composite shows a slightly larger discharge time, reflecting improved capacitance, but the difference compared to pure MXene is modest. This limited improvement may arise from the relatively low MXene loading in the PVA matrix, followed by the carbonization step. Additionally, the longer charging time compared to discharge can be attributed to slower ion adsorption kinetics and redistribution during the charging process, which is typical in pseudocapacitive systems.[21] The specific capacitance (C_s), as determined from eqn (S3), was 1084.2 F g^{-1} for Cr_2CT_x/carbon nanofiber and 894.5 F g^{-1} for pristine Cr_2CT_x. The energy density and power density were determined using eqn (S4) and (S5), were 21.74 Wh kg^{-1} and 379.9 W kg^{-1} for the composite,

respectively. Meanwhile, the Cr_2CT_x MXene delivered 21.23 Wh kg^{-1} and 436.7 W kg^{-1}, respectively. Fig. 2c demonstrates the GCD profile of Cr_2CT_x/carbon nanofiber recorded at different current densities varying from 1–10 A g^{-1}. The improved charge–discharge performance is mainly attributed to the increased surface area and interconnected network, which enable more efficient charge transfer. Additionally, the Nyquist plot with the fitted Randles circuit (Fig. 2d) supports these observations, showing a lower R_{ct} of 1.10 Ω for Cr_2CT_x/carbon nanofiber compared to 1.67 Ω for pristine MXene, indicating faster interfacial kinetics. Shown in Fig. 2e, the electrode retained 86% of its capacitance after 5000 charge–discharge cycles at 20 A g^{-1} and 83% for Cr_2CT_x, demonstrating that the composite effectively maintains its morphology (Fig. 2e, inset) alongside its structural features, a slight decrease in peak intensity and the appearance of additional peaks attributable to the Ni foam substrate used for the working electrode are observed (Fig. S4). The MXene peak is retained in the XRD, along with the amorphous carbon peak at lower intensity. While MXene restacking may limit performance, this can potentially be mitigated by dispersing and isolating single MXene flakes; however, this is a challenging process that requires further optimization and study. While Cr_2CT_x/carbon nanofiber retained its initial capacitance, underscoring its excellent cycling stability and promise for long-term energy storage applications.

An asymmetric supercapacitor device was assembled using Cr_2CT_x/carbon nanofiber as the active electrode and activated carbon as the counter electrode, with 3 M KOH serving as the electrolyte. Cyclic voltammetry profiles (Fig. 3a), recorded within a potential window of 0–1.4 V at scan rates ranging from 10 to 100 mV s^{-1}, exhibited a quasi-rectangular shape at lower scan rates, indicating dominant EDLC behavior contributed by the activated carbon electrode. Notably, the composite contributed pseudocapacitive behavior, as evidenced by subtle redox features in the CV curves, which can be ascribed to the redox-active surface groups on Cr_2CT_x and the porous nanofibrous architecture. The CV curves' symmetry about the zero-current axis indicates highly reversible charge–discharge behavior. The GCD curves (Fig. 3b) displayed near-triangular shapes with slight nonlinearity, confirming the combined EDLC and pseudocapacitive behavior. The Cr_2CT_x/carbon nanofiber composite achieved a high C_s of 338.8 F g^{-1} at 1 A g^{-1} in the two-electrode system. The device achieved a notable energy density of 67.7 Wh kg^{-1}, and power density of 1998 W kg^{-1}, underscoring its potential for high-performance energy storage systems. The Nyquist plot (Fig. 3c), revealed a R_{ct} of 14.46 Ω, indicative of enhanced electrical conductivity and efficient transfer at the electrode–electrolyte interface. Furthermore, the stability analysis (Fig. 3d) revealed that the device retained 91% of its initial capacitance after 5000 charge–discharge cycles at a 10 A g^{-1}, confirming its strong durability and long-term electrochemical stability.

Additionally, a comparison table (Table S3) is provided to benchmark our Cr_2CT_x MXene results against available studies on Cr_2CT_x and other MXene-based carbon nanofiber composites for supercapacitance application.

In summary, the Cr_2CT_x/carbon nanofiber composite was prepared *via* electrospinning using a green, low-cost, non-conducting PVA polymer. MXene incorporation enhanced conductivity, surface area, and charge storage. The synergy of high conductivity and surface redox activity of MXene with the porous scaffold ensures mechanical stability, accelerates ion diffusion, and minimizes MXene restacking. The robust nanofibrous carbon network demonstrated excellent supercapacitor performance, delivering a capacitance of 338.8 F g^{-1}, remarkable capability, and efficient cycling stability with 91% retention over 5000 cycles, underscoring its promise as a next-generation material for advanced energy storage systems. The future work can explore flexible, wearable devices and optimized MXene loading to enhance performance and practical applicability in sustainable energy.

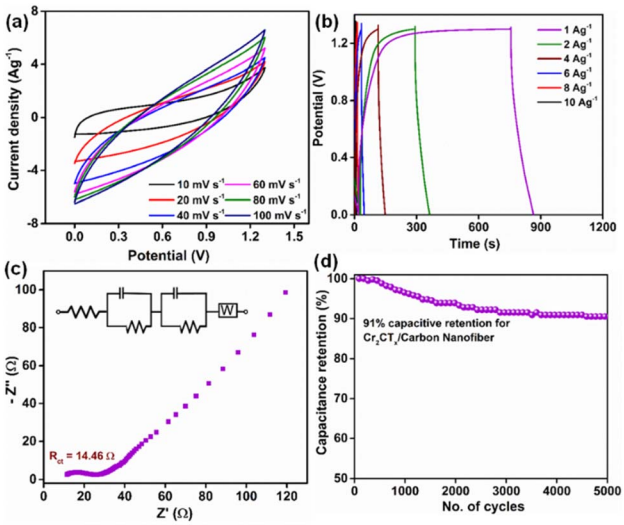

Fig. 3 (a) CV curve, (b) GCD plot, (c) Nyquist plot and (d) cycling durability test of Cr_2CT_x/carbon nanofiber using a two-electrode system.

Author contributions

Madhushree R.: conceptualization, investigation, data curation, methodology, formal analysis, writing the original draft. Sunaja Devi K. R.: conceptualization, supervision, visualization, formal analysis, writing – review and editing. Chaithra K. P.: methodology, formal analysis. Vinod T. P.: supervision, formal analysis, writing – review and editing. B. Saravanakumar: data curation, formal analysis.

Conflicts of interest

The authors declare no conflict of interest.

Data availability

The data that support the findings of this study are available from the corresponding author, [K. R. Sunajadevi, sunajadevi.kr@christuniversity.in], upon reasonable request. Due to

confidentiality agreements and ethical considerations, the data are not publicly available.

The supplementary information (SI) file provides additional information, including materials characterization, experimental procedures, and supporting figures. Supplementary information: XRD, Raman, BET–BJH, FTIR, SEM images, elemental mapping, TGA profiles, electrode fabrication details, post-analysis characterization, and a comparison table with previous reports is available. See DOI: **https://doi.org/10.1039/d5na00753d**.

Notes and references

1 X. Hong, J. He, C. Duan, G. Wang and B. Liang, *Renew. Sustain. Energy Rev.*, 2025, **209**, 115134.
2 S. Mathew, R. Madhushree and K. R. Sunaja Devi, *Sustain. Energy Fuels*, 2023, **7**, 2601–2612.
3 Z. W. Seh, K. D. Fredrickson, B. Anasori, J. Kibsgaard, A. L. Strickler, M. R. Lukatskaya, Y. Gogotsi, T. F. Jaramillo and A. Vojvodic, *ACS Energy Lett.*, 2016, **1**, 589–594.
4 R. Madhushree and K. R. Sunajadevi, *Dalton Trans.*, 2025, **54**(16), 6653–6664.
5 M. Pandey, K. Deshmukh, A. Raman, A. Asok, S. Appukuttan and G. R. Suman, *Renew. Sustain. Energy Rev.*, 2024, **189**, 114030.
6 A. S. Levitt, M. Alhabeb, C. B. Hatter, A. Sarycheva, G. Dion and Y. Gogotsi, *J. Mater. Chem. A*, 2019, **7**, 269–277.
7 T. Zhao, D. Yang, S. M. Hao, T. Xu, M. Zhang, W. Zhou and Z. Z. Yu, *J. Mater. Chem. A*, 2022, **11**, 1742–1755.
8 Z. Guo, Y. Li, Z. Lu, Y. Chao and W. Liu, *J. Mater. Sci.*, 2022, **57**, 3613–3628.
9 T. Kshetri, D. D. Khumujam, T. I. Singh, Y. S. Lee, N. H. Kim and J. H. Lee, *Chem. Eng. J.*, 2022, **437**, 135338.
10 H. Hwang, S. Byun, S. Yuk, S. Kim, S. H. Song and D. Lee, *Appl. Surf. Sci.*, 2021, **556**, 149710.
11 S. Xue Yan, S. Hua Luo, Q. Wang, Y. Hui Zhang and X. Liu, *Composites, Part B*, 2021, **224**, 109246.
12 K. Donthula, U. R. Malothu, R. Araga, R. Vooradi, V. S. Patnaikuni, M. V. Reddy and M. Kakunuri, *Polym. Compos.*, 2023, **44**, 7571–7584.
13 G. P. Awasthi, B. Maharjan, S. Shrestha, D. P. Bhattarai, D. Yoon, C. H. Park and C. S. Kim, *Colloids Surf., A*, 2020, **586**, 124282.
14 A. S. Levitt, M. Alhabeb, C. B. Hatter, A. Sarycheva, G. Dion and Y. Gogotsi, *J. Mater. Chem. A*, 2019, **7**, 269–277.
15 R. Madhushree, K. P. Chaithra, K. R. Sunaja Devi and T. P. Vinod, *New J. Chem.*, 2024, **48**, 17159–17166.
16 M. Shahbaz, N. Sabir, N. Amin, Z. Zulfiqar and M. Zahid, *Front. Chem.*, 2024, **12**, 1413253.
17 B. S. Reghunath, S. D. K R, S. Rajasekaran, B. Saravanakumar, J. J. William and D. Pinheiro, *Electrochim. Acta*, 2023, **461**, 142685.
18 Y. Li, G. Zhao, Y. Qian, J. Xu and M. Li, *J. Mater. Sci. Technol.*, 2018, **34**, 466–471.
19 A. Iqbal and N. M. Hamdan, *Materials*, 2021, **14**(21), 6292.
20 D. Gandla, F. Zhang and D. Q. Tan, *ACS Omega*, 2022, **7**, 7190–7198.
21 M. Heydari Gharahcheshmeh and K. Chowdhury, *Energy Adv.*, 2024, **3**, 2668–2703.